S-factor of $^{14}N(p, \gamma)^{15}O$ at astrophysical energies[⋆]

G. Imbriani[1,a], H. Costantini[2], A. Formicola[3], A. Vomiero[4], C. Angulo[5], D. Bemmerer[6], R. Bonetti[7], C. Broggini[6], F. Confortola[2], P. Corvisiero[2], J. Cruz[8], P. Descouvemont[9], Z. Fülöp[10], G. Gervino[11], A. Guglielmetti[7], C. Gustavino[3], Gy. Gyürky[10], A.P. Jesus[8], M. Junker[3], J.N. Klug[12], A. Lemut[2], R. Menegazzo[6], P. Prati[4], V. Roca[1], C. Rolfs[12], M. Romano[1], C. Rossi-Alvarez[6], F. Schümann[12], D. Schürmann[12], E. Somorjai[10], O. Straniero[13,14], F. Strieder[12], F. Terrasi[15,14], and H.P. Trautvetter[12]

1 Università di Napoli "Federico II", Dipartimento di Fisica and INFN, Napoli, Italy
2 Università di Genova, Dipartimento di Fisica and INFN, Genova, Italy
3 Laboratori Nazionali del Gran Sasso dell'INFN, Assergi, Italy
4 Università di Padova, Dipartimento di Fisica and INFN, Legnaro, Italy
5 Centre de Recherches du Cyclotron, Université Catholique de Louvain, Louvain-la-Neuve, Belgium
6 INFN, Padova, Italy
7 Università di Milano, Dipartimento di Fisica and INFN, Milano, Italy
8 Centro de Física Nuclear da Universidade de Lisboa, Lisboa, Portugal
9 Physique Nucléaire Théorique et Physique Mathématique, CP 229, Université Libre de Bruxelles, Brussels, Belgium
10 Atomki, Debrecen, Hungary
11 Università di Torino, Dipartimento di Fisica Sperimentale and INFN, Torino, Italy
12 Ruhr-Universität Bochum, Institut für Physik mit Ionenstrahlen, Bochum, Germany
13 Osservatorio Astronomico Collurania, Teramo, Italy
14 INFN, Napoli, Italy
15 Seconda Università di Napoli, Dipartimento di Scienze Ambientali, Caserta, Italy

Abstract. The astrophysical $S(E)$ factor of $^{14}N(p, \gamma)^{15}O$ has been measured for effective center-of-mass energies between $E_{eff} = 119$ and 367 keV at the LUNA facility using TiN solid targets and Ge detectors. The data are in good agreement with previous and recent work at overlapping energies. R-matrix analysis reveals that due to the complex level structure of ^{15}O the extrapolated $S(0)$ value is model dependent and calls for additional experimental efforts to reduce the present uncertainty in $S(0)$ to a level of a few percent as required by astrophysical calculations.

1 Introduction
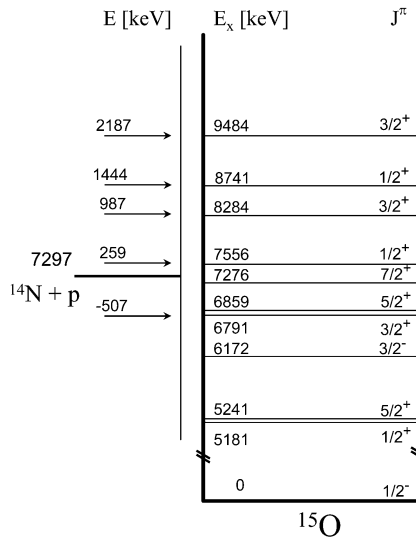
The capture reaction $^{14}N(p, \gamma)^{15}O$, the slowest process in the hydrogen burning CNO cycle [1], is of high astrophysical interest as its reaction rate influences sensitively the age determination of globular clusters [2] and the solar neutrino spectrum [3,4]. The capture cross-section needs to be known down to $E_0 = 30$ keV (the Gamow peak in core H-burning stars), which is far below the low-energy limit of direct γ-ray measurements, *i.e.* the center-of-mass

energy $E = 240$ keV[1] [5]. Thus, the data had to be extrapolated over a large energy gap leading to a substantial uncertainty for the astrophysical S-factor at zero energy, $S(0)$. According to the data and analyses of Schröder *et al.* [5], there are two major and nearly equal contributions to $S(0)$: the direct capture (DC) to the 6.79 MeV state in ^{15}O and the capture to the ground state (gs) in ^{15}O. The latter process is enhanced due to a subthreshold resonance at $E_R = -507$ keV (fig. 1), the width of which was taken as a free parameter in the fit [5]. The extrapolation led to $S_{tot}(0) = 3.20 \pm 0.54$ keV b, with $S_{gs}(0) = 1.55$ keV b and $S_{6.79}(0) = 1.41$ keV b.

---

1 In this work all proton energies are taken in the center-of-mass system, except where quoted differently.

E [keV] E_x [keV] J^{π}

2187 →   9484 $3/2^+$

1444 →   8741 $1/2^+$
987 →   8284 $3/2^+$

7297   259 →   7556 $1/2^+$
^{14}N + p   7276 $7/2^+$
                -507 →   6859 $5/2^+$
                             6791 $3/2^+$
                             6172 $3/2^-$

                             5241 $5/2^+$
                             5181 $1/2^+$

                             0              $1/2^-$

^{15}O

Fig. 1. Relevant level scheme of ^{15}O near the ^{14}N(p, γ)^{15}O threshold.

Subsequently, the data of Schröder *et al.* [5] were analyzed by Angulo and Descouvemont [6] using an *R*-matrix approach [7]. Contrary to the extrapolation by Schröder *et al.* [5] for capture to the ground state, they reported a negligible contribution $S_{gs}(0) = 0.08$ keV b due to a smaller total width of the subthreshold resonance and thus they suggested $S_{tot}(0) = 1.77 \pm 0.20$ keV b. A smaller width of the 6.79 MeV state was supported by a lifetime measurement via the Doppler-shift method [8] and by a Coulomb excitation measurement [9].

Both $S_{gs}(0)$ and $S_{6.79}(0)$ are dominated by $E1$ capture mechanisms. Based on a measurement of the analysing power at $E_p = 270$ keV, Nelson *et al.* [10] reported a small contribution (about 4%) of an $M1$ capture to the overall capture process, but this single data point did not significantly improve the situation. The available data clearly demonstrate the large uncertainty affecting the extrapolations over a large energy gap in a nucleus, such as ^{15}O, with a complex level structure, a problem calling for new direct γ-ray measurements towards lower energies.

The LUNA (Laboratory Underground for Nuclear Astrophysics) Collaboration started in 2001 a reinvestigation of ^{14}N(p, γ)^{15}O (using TiN solid targets and Ge detectors) with a particular emphasis on $S_{gs}(E)$. The data obtained down to $E_p = 140$ keV [11] confirmed the small contribution of the ground-state capture giving $S_{tot}(0) = 1.7 \pm 0.1 \pm 0.2$ keV b. The *R*-matrix analysis of these low-energy data included the high-energy data of Schröder *et al.* [5] and the results of the ANC (Asymptotic Normalization Coefficient) method [12,13]. At the completion of the LUNA work, another set of low-energy data became available at $E_p = 155$ to 524 keV [14], which is in excellent agreement with the LUNA data in the overlapping energy range. Here, we report on the LUNA solid target work, while additional details can be found in [15–17].
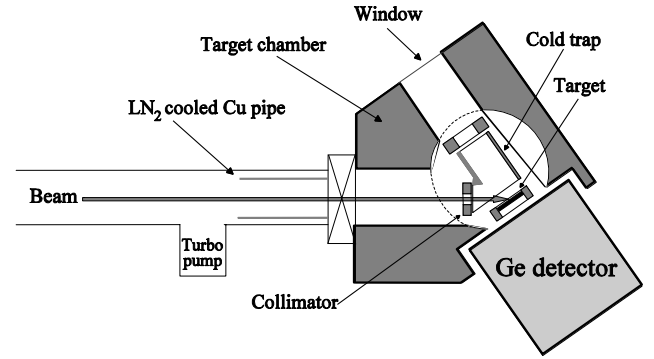
Fig. 2. Schematic diagram of the setup used in geometry 1.

2 Experimental apparatus

2.1 Accelerator

The 400 kV LUNA accelerator [18] provided a proton beam on target of up to 500 μA. The absolute beam energy was known with an accuracy of 300 eV, and the energy spread and the long-term energy stability were observed to be 100 eV and 5 eV/h, respectively. The beam current on target was monitored by a current integrator with an estimated uncertainty of 2%. The targets were directly water-cooled. In the target chamber (fig. 2) the target ladder was surrounded by an electrically insulated collimator biased to -300 V to suppress secondary electrons. A uniform rectangular beam spot (4 by 4 cm) was produced within the target area by magnetic wobbling of the beam. In order to prevent build-up of impurities on the target, a LN$_2$-cooled Cu cold finger was used.

2.2 Detectors and electronics

The laboratory's 1400 m rock cover reduces the background rate in the Ge detectors by more than three orders of magnitude at $E_\gamma > 5$ MeV [19] compared with a detector placed at the surface of the Earth. It is in this E_γ region that the capture γ-ray lines of secondary transitions (5.18, 6.17, and 6.79 MeV) and the ground-state transition (about 7.5 MeV) are located (fig. 1). In the experiments two different setups were used:

Geometry 1 (fig. 2): The target was oriented with its normal at 55° with respect to the beam direction. The capture γ-rays were observed with a HPGe-detector (126% relative efficiency), whose front face and target were parallel with a distance $d = 1.5$ cm. The detector was surrounded by 5 cm of lead, which reduced the background in the low-energy range of the primary transitions by a factor of 10. The setup was used for the measurement of excitation functions, while for the determination of the detector efficiency and of summing effects the distance between target and detector was increased in discrete steps up to $d = 20.5$ cm.

Geometry 2: The target normal was oriented at 19° with respect to the beam direction. Using a different target chamber three HPGe-detectors were positioned

around the target: the 126% detector was placed at 0°, while the other two detectors (120% and 108% relative efficiencies) were placed at 90° and 125°. The distance between the detector end cap and the target was 7 cm for all detectors. The setup was used in the measurement of Doppler shifts, excitation energies, and angular distributions.

2.3 Targets

The ^{14}N solid targets had to fulfill several requirements: i) uniform depth distribution starting at the surface, ii) thickness large enough that possible sputtering effects at low energies and over long running times were negligible for the yield measurements, iii) stability against high beam power, and iv) low concentration of impurities of light elements. The targets were produced either by implantation of a ^{14}N ion beam into a suitable backing, or by evaporation of a Ti layer on a specific backing and heating in a N_2 atmosphere, or by sputtering of TiN on a backing. The resulting quality of the targets was investigated using the $E_R = 259$ keV resonance. Figure 3 shows the results out of a large number of tests [15] performed with different backings and target thicknesses. The evaporated and sputtered targets showed a steep rise in the excitation function at the resonance energy, with a slope comparable to the convolution of beam resolution and resonance width. In the implanted target the surface region was not saturated. The step heights to the plateau were similar for all targets indicating a similar stoichiometry at saturation. Our conclusion was that the sputtered targets of TiN (with a typical thickness of 80 keV, Ta-backing) had the most uniform number density profile and could withstand many days of intense beam bombardment without a significant deterioration. Typically, a new TiN target was installed after a running time of 1 week, which corresponded to an accumulated charge of about 200 C. During this time we observed a small decrease of the plateau-yields due to the proton implantation (insert of fig. 3). The stoichiometry of the TiN layer —used for the determination of the strength of the $E_R = 259$ keV resonance— was measured via Rutherford Backscattering Spectrometry using a 2.0 MeV ^{4}He beam in the INFN National Laboratory of Legnaro, resulting in Ti/N = 1/(1.08 ± 0.05). To measure the capture cross-section above the $E_R = 259$ keV resonance we used evaporated targets, since we needed here thinner targets to minimize the influence of the resonance: their absolute stoichiometry did not need to be precisely known because of the normalization procedure adopted (sect. 3.5).

2.4 Beam-induced background

The presence of light-element impurities can produce intense γ-ray background lines due to their relatively low Coulomb barrier and/or high cross-sections. In particular, γ-lines from reactions on ^{11}B, ^{12}C, ^{13}C, ^{18}O and ^{19}F have been investigated and their intensity was minimized by
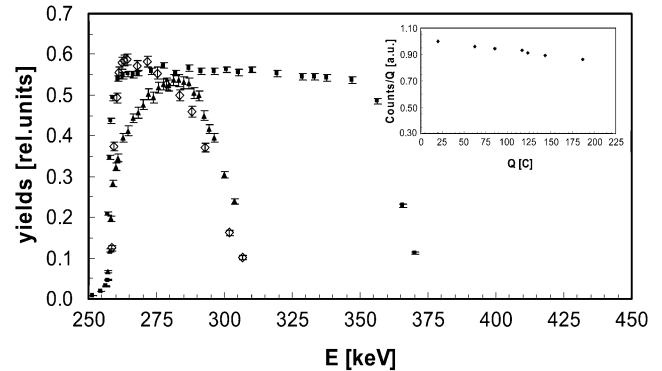
Fig. 3. Excitation function of ^{14}N(p, γ)^{15}O near the $E_R = 259$ keV resonance using different targets: squares = sputtered target, triangles = implanted target, diamonds = evaporated target. The insert shows the thick-target yield as a function of accumulated charge Q on the sputtered target.

a proper choice of target backing and preparation procedures [20], where the sputtered target was best. A sample γ-ray spectrum obtained at $E_p = 250$ keV is shown in fig. 4: the primary capture transitions (*e.g.*, tr $\rightarrow$ 6.79) and the secondary transitions (*e.g.*, 6.79 $\rightarrow$ 0) as well as background lines (identified by their impurity nuclides) are indicated. The high-energy part of the spectrum obtained at $E_p = 140$ keV, our lowest bombarding energy, is shown in fig. 5: the primary transition tr $\rightarrow$ 0 and nearly all secondary transitions are clearly observable.

3 Experimental procedures, data analyses and results
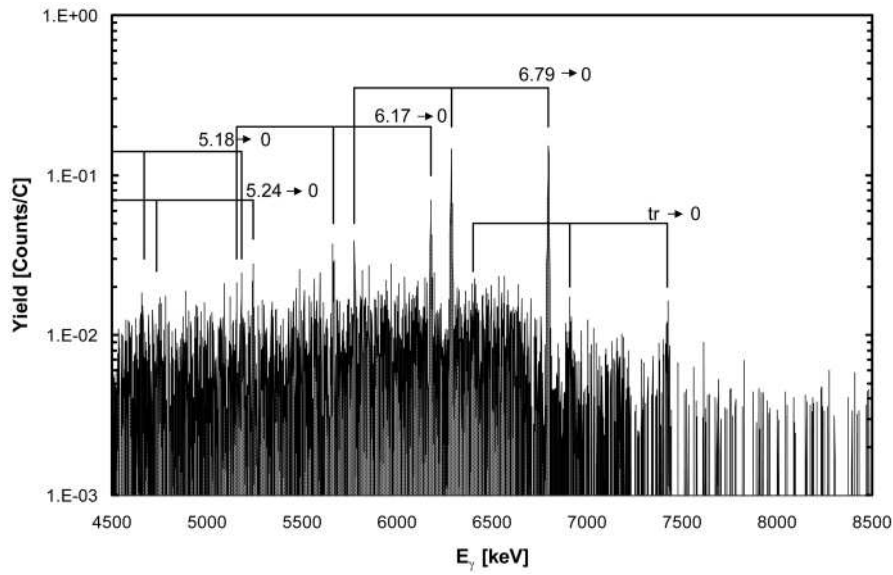
3.1 Excitation energies in ^{15}O

The energy scale of the Ge detectors used in geometry 2 was determined using the well-known background lines from ^{232}Th, ^{40}K and ^{214}Bi and the ground-state capture transition at the resonance. The latter energy was calculated from the known accelerator energy ($E_R = 259.4 \pm 0.3$ keV, sect. 3.3) and the Q value of ^{14}N(p, γ)^{15}O ($Q = 7296.8 \pm 0.5$ keV [21]), where effects of the Doppler shift and recoil energy were taken into account: $E_x = 7556.4 \pm 0.6$ keV. The energies of the $\gamma\gamma$ cascades via the 5.18, 6.17 and 6.79 MeV states were then used to determine the excitation energies of these states, where the Doppler attenuation factors were left as a free parameter in the fit. The results are summarised in table 1 and are in good agreement with previous work [21].

3.2 Efficiency and summing effects

Due to i) the close geometry of the setup in geometry 1 (fig. 2), ii) the cascade structure of the capture process, and iii) the small branching to the ground state, the "summing-in" effect (*i.e.* the cascade γ-rays giving a contribution to the ground-state full-energy peak) and the
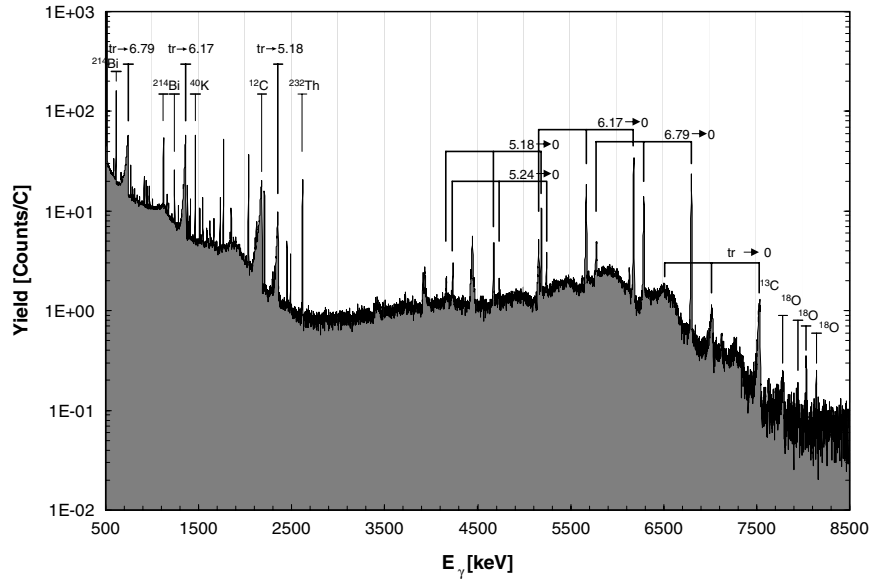
Fig. 4. Spectrum obtained at $E_p = 250$ keV in geometry 1 over an accumulated charge of 87 C. The background above $E_\gamma = 8$ MeV is mainly due to a small ^{11}B contamination.

Fig. 5. Spectrum obtained at $E_p = 140$ keV in geometry 1 over an accumulated charge of 210 C.

Table 1. Excitation energies of ^{15}O states and low energy at the $E_R = 259$ keV resonance.

E_X [keV]		Branching [%]		
Present work	[21]	Present work	[21]	[14]
5180.8 ± 0.2	5183.0 ± 1.0	17.1 ± 0.2	15.8 ± 0.5	17.3 ± 0.2
	5240.9 ± 0.3	0.6 ± 0.3		
6172.3 ± 0.2	6173.3 ± 1.7	57.8 ± 0.3	57.5 ± 0.6	58.3 ± 0.5
6791.7 ± 0.2	6793.3 ± 1.7	22.9 ± 0.3	23.2 ± 0.4	22.7 ± 0.3
7556.4 ± 0.6	7556.5 ± 0.4	1.6 ± 0.1	3.5 ± 0.6	1.70 ± 0.07

"summing-out" effect (*i.e.* a full-energy detection of one cascade γ-ray and any concurrent interaction of the other member of the cascade) have to be taken into account. For the efficiency and summing-effect evaluation, we considered γ-ray spectra obtained at 55° for different distances d from the target (*i.e.* $d = 1.5$, 5.5, 10.5, and 20.5 cm). The spectra involved ^{137}Cs and ^{60}Co calibrated sources placed at the target position as well as the spectra obtained at the $E_R = 259$ keV resonance. The dependence of the full-energy efficiency ε_{fe} on the γ-ray energy E_γ and on the distance d were parameterized by the following functions [22]:

$$\ln\left(\varepsilon_{fe}\right) = a + b\ln(E_\gamma) + c[\ln(E_\gamma)]^2 , \qquad (1)$$

$$\varepsilon_{fe}(d) = \frac{1 - e^{\frac{d+d_0}{1+\beta\sqrt{E_\gamma}}}}{(d+d_0)^2} . \qquad (2)$$

In order to take into account the summing-in and summing-out effects, the following expressions were used:

$$Y_{gs} = R\left(b_{gs}\varepsilon_{fe}(E_{gs}) + \sum_i b_i\varepsilon_{fe}(E_i^{sec})\varepsilon_{fe}(E_i^{pri})\right) ,$$

$$Y_{i_{pri}} = Rb_i\varepsilon_{fe}(E_{i_{pri}})(1 - \varepsilon_{tot}(E_{i_{sec}})) ,$$
$$Y_{i_{sec}} = Rb_i\varepsilon_{fe}(E_{i_{sec}})(1 - \varepsilon_{tot}(E_{i_{pri}})) , \qquad (3)$$

where Y_{gs}, $Y_{i_{pri}}$ and $Y_{i_{sec}}$ are the observed yields of the ground-state transition and of the transitions through the energy level i; the subscripts *pri* and *sec* refer to primary and secondary transitions, respectively; R is the number of reactions per unit charge, b_{gs} and b_i are the branchings, ε_{fe} and ε_{tot} are the full energy and total efficiencies, respectively. Equation (3) assumes isotropic angular distributions and correlations. In these equations the total detection efficiency is parameterized as [22]

$$\ln\left(\frac{\varepsilon_{fe}}{\varepsilon_{tot}}\right) = K_1 + K_2\ln(E_\gamma) + K_3(\ln(E_\gamma))^2 . \qquad (4)$$

Each excited state that is fed by the resonance then decays to the ground state with a 100% probability: this allows to set constraints on the efficiency curve arising from the one-by-one equality of the intensities of primary and secondary transitions involving each excited state:

$$\frac{Y_{i_{pri}}}{Y_{i_{sec}}} = \frac{\varepsilon_{fe}(E_{i_{pri}})(1 - \varepsilon_{tot}(E_{i_{sec}}))}{\varepsilon_{fe}(E_{i_{sec}})(1 - \varepsilon_{tot}(E_{i_{pri}}))} . \qquad (5)$$

These constraints were used in a global fit to the data. The free parameters are the coefficients in the parameterizations (eqs. (1), (2) and (4)) and the four branching ratios of the resonance. Figure 6 shows the behavior of the efficiency $\varepsilon_{fe}(E)$ *versus* energy for the four distances: the data points are those from the reaction (diamonds) and from the sources (squares) and the lines are the fit. Points and data refer to distances of 1.5, 5.5, 15.5 and 20.5 cm starting from the highest curve, respectively. In order to illustrate the importance of the summing correction, the crosses in the figure represent the values of the efficiency at the closest distance which would be obtained neglecting the summing effects: note the large deviation for the ground-state capture at 7.5 MeV. The results
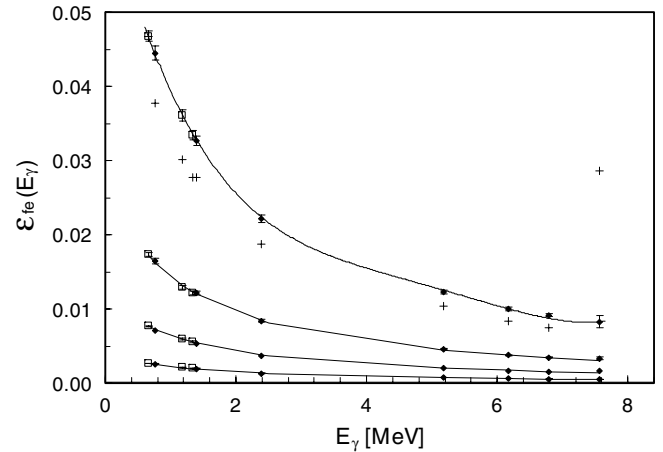
Fig. 6. Full-energy peak efficiency as a function of γ-ray energy for the geometry 1 with distances $d = 1.5$, 5.5, 15.5, and 20.5 cm, from top to bottom. The lines through the data points are the results from a fit. The crosses are the results omitting the summing effects.

shown in fig. 6 are consistent with values obtained from Monte Carlo simulations [16].

The resulting branchings of the $E_R = 259$ keV resonance are in good agreement with previous work [21] (table 1) except for the ground-state decay.

3.3 Strength, energy and width of the $E_R = 259$ keV resonance

The thick-target yield Y^∞ of the resonance is given by the expression [1]

$$Y^\infty = \frac{\lambda^2}{2}\frac{\omega\gamma}{\eta(E)} , \qquad (6)$$

where $\eta(E) \equiv dE/dx$ is the stopping power of the target at the resonance energy. For the observed stoichiometry of the TiN target, the compilation [23] leads to a stopping power $\eta(E_R) = 32.8$ eV/$(10^{15}$ atoms/cm$^2)$. We find then a resonance strength $\omega\gamma = 12.9 \pm 0.4$ (stat) ± 0.8 (sys) meV. The systematic error arises mainly from the uncertainty in the stopping power and the accuracy of the current measurement. The strength value is in good agreement with previous work: $\omega\gamma = 14 \pm 1$ meV [21] and $\omega\gamma = 13.5 \pm 1.2$ meV [14].

In the energy region of the $E_R = 259$ keV resonance, the yield of a capture transition as a function of beam energy E is given by the integral

$$Y(E) = \int_0^E \frac{\sigma(E)}{\eta(E)}dE . \qquad (7)$$

With the known stopping power and assuming the cross-section as an incoherent sum of a constant non-resonant term plus a Breit-Wigner term, we have fitted the experimental curves of all four primary capture transitions, where the free parameters were E_R and Γ_R. The results for all four transitions (fig. 7) were within their
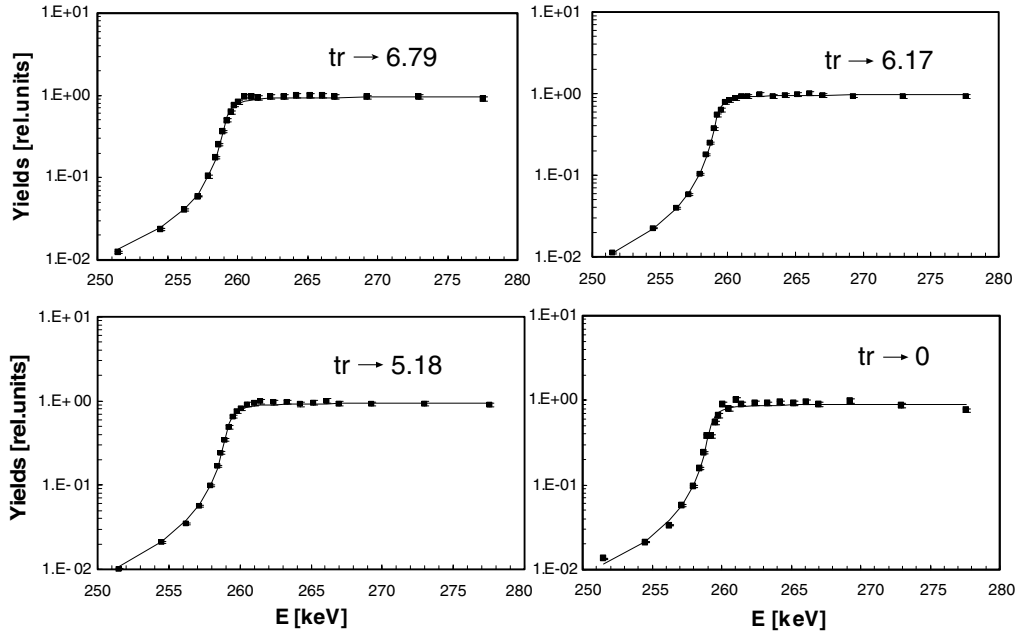
Fig. 7. Excitation functions of the 4 primary transitions near the $E_R = 259$ keV resonance. The lines through the data points are the result of a fit.

respective errors leading to $E_R = 259.4 \pm 0.3$ keV and $\Gamma_R = 0.96 \pm 0.05$ keV, in good agreement with previous work [5,21].

3.4 Angular distributions

Angular distributions were measured using geometry 2 at energies $E = 206$, 313, and 361 keV. Since the $J^\pi = 1/2^+$, $E_R = 259$ keV resonance exhibits isotropic distributions, the relative efficiencies of the Ge detectors were measured at this resonance. The resulting distributions were fitted with Legendre polynomials

$$W(\theta) = 1 + a_1 Q_1 P_1(\theta) + a_2 Q_2 P_2(\theta), \qquad (8)$$

where a_k are the angular distribution coefficients and Q_k the attenuation coefficients calculated according to [24]. Within experimental uncertainties, all primary and secondary transitions are isotropic [16] and consistent with the results of Schröder *et al.* [5]. As known from [5], the exception is the primary transition to the 6.79 MeV state, which exhibits a $\sin^2(\theta)$ distribution ($a_2 = -0.50$): $a_2 = -0.79 \pm 0.11$, -0.64 ± 0.06, and -0.57 ± 0.07 at $E = 206$, 313, and 361 keV, respectively, consistent with the data from [5] at higher energies.

3.5 Primary peaks

Excitation functions have been obtained at proton energies between $E_p = 140$ and 400 keV for all primary transitions. The observed line-shape of a primary transition is determined by the cross-section behavior $\sigma(E_p)$ in the proton energy interval spanned by the incident beam during

the slowing-down process in the target, once the transformation from the energy E_p (at which the reaction takes place) to the corresponding γ-ray energy $E_\gamma = E + Q - E_x$ is performed. The shape is also influenced by the energy loss of the protons in the thick target, since the stopping power of the protons in TiN is a function of proton energy [25]. Finally, the position of the high-energy rise in the line-shape is influenced by the Doppler effect and the recoil of the compound nucleus.

The number of counts N_i in channel i of the γ-spectrum, corresponding to the energy bin $E_{\gamma i}$ to $E_{\gamma i} + \delta E_\gamma$ (δE = dispersion in units of keV per channel) is given by the expression

$$N_i = \frac{\sigma(E_{pi})\delta E_\gamma \varepsilon_{fe}(E_{\gamma i}) b_j}{\eta(E_p i)} \qquad (9)$$

for $E_{pi} \leq E_p$ (E_{pi} = proton energy corresponding to channel i, E_p = incident proton energy), where $\sigma(E_{pi})$ is the capture cross-section, $\varepsilon_{fe}(E_{\gamma i})$ is the γ-ray detection efficiency, and b_j is the branching of the associated decay. The conversion from $E_{\gamma i}$ to E_{pi} includes the Doppler and recoil effects. The result is folded with the known detector resolution ΔE_γ to obtain the experimental line-shape. The spectrum obtained at an energy E_p was compared to that obtained with the same target at the $E_R = 259$ keV resonance energy: the comparison was performed before and after a given run at E_p, where the thick-target resonance yields Y^∞ were averaged. In this comparison the experimental fit-quantity is the ratio

$$\frac{N_i}{Y^\infty} = \frac{2\sigma(E_{pi})\delta E_\gamma \varepsilon_{fe}(E_{\gamma i}) b_j \eta(E_{Rlab})}{\lambda^2 \omega\gamma b_{Rj}\varepsilon_{fe}(E_{R\gamma})\eta(E_{pi})} . \qquad (10)$$

The energy dependence of the full-energy efficiency is known; the summing-out correction for the cascade
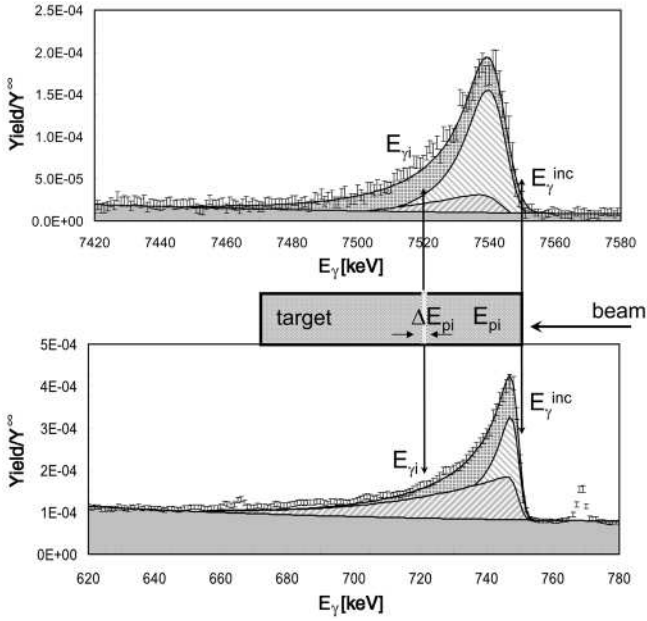
Fig. 8. Gamma-ray spectra near the ground-state transition (top) and the primary transition to the 6.79 MeV state (bottom) obtained at $E_p = 250$ keV (for details, see text).

Fig. 9. Overlay of spectra near the primary transition to the 6.79 MeV state obtained at $E_p = 250$ and 240 keV (top) and the difference of both spectra (center). The bottom part shows a fit using the R-matrix analysis result.

transitions via the three excited states is smaller than 1%; the summing-in correction for the capture to the ground state depends on b_j and b_{Rj}. Thus, for the ground-state capture a correction has to be applied which can be obtained replacing eq. (10) with
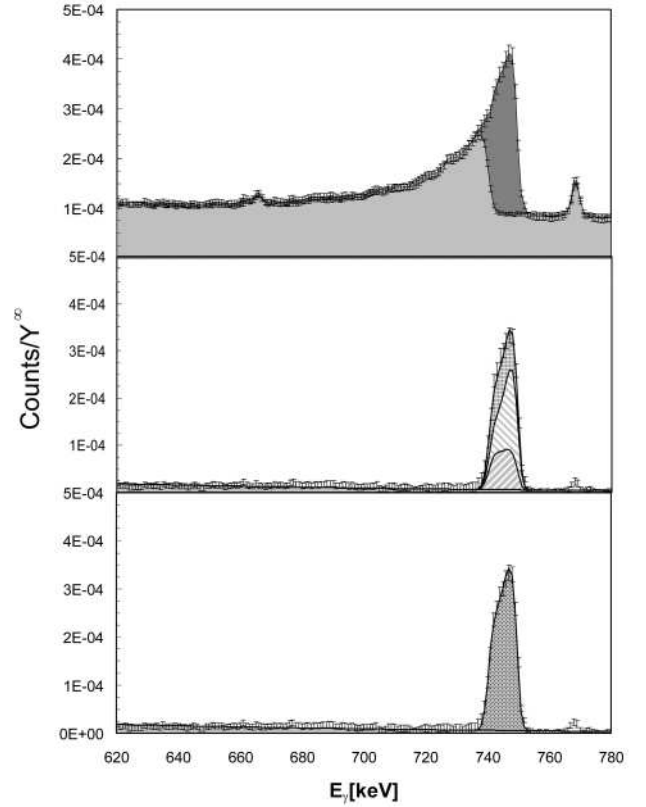
$$\frac{N_{gs}}{Y_{gs}^\infty} \propto$$

$$\frac{\sigma_{gs}(E_p)\varepsilon_{fe}(E_\gamma^{gs}) + \sum_i \sigma_i(E_p)\varepsilon_{fe}(E_{\gamma i}^{sec})\varepsilon_{fe}(E_{\gamma i}^{pri})}{\sigma_{gs}(E_{Rp})\varepsilon_{fe}(E_{\gamma R}^{gs}) + \sum_i \sigma_i(E_{Rp})\varepsilon_{fe}(E_{\gamma Ri}^{sec})\varepsilon_{fe}(E_{\gamma Ri}^{pri})}$$

$$(11)$$

using $\sigma_i(E_p)$ deduced from eq. (10).

The summing-in correction for the ground-state transition is not negligible and becomes increasingly uncertain with decreasing proton energy. This was the main reason why we stopped the measurements at $E_p = 140$ keV although from a statistical point of view and background considerations we could go lower in energy (fig. 5). In the case of the other capture transitions the summing-out correction depends only on the precision of the efficiency curve.

The last step in the analysis of the primary peaks is to introduce the function for the cross-section in eq. (10). Since we have analysed the cross-section above and below the $E_R = 259$ keV resonance, we have written —in first approximation— the cross-section as an incoherent sum of a non-resonant term, which assumed a constant astrophysical $S(E)$ factor S_{NR}, and a resonant term described by the Breit-Wigner formula

$$\sigma(E_{p_i}) = \frac{S_{NR}e^{-2\pi\eta}}{E_{p_i}} + \frac{\lambda^2}{\pi}\omega\gamma\frac{\Gamma}{(E_{p_i} - E_R)^2 + (\Gamma/2)^2} .$$

$$(12)$$

These expressions were fitted to the γ-ray spectrum yields, superimposed on an exponential background.

An example of this fitting procedure is given in fig. 8, where the γ-spectra in the region of the ground-state transition (top figure) and of the primary transition to the 6.79 MeV state (bottom figure) are shown as obtained at $E_p = 250$ keV: the gray area is the background, the left-oriented stripes area and the right-oriented stripes area represent the non-resonant and resonant parts of the cross-section, respectively, and the squared area is their sum. In the fits we used as free parameters the non-resonant astrophysical factor and the background parameters. After the R-matrix analysis (sect. 4) this procedure has been checked resulting in a fit shown at the bottom of fig. 9 for the transition to the 6.79 MeV state.

Since the non-resonant astrophysical $S(E)$ factor can be considered as constant only in a short energy range, our thick target may represent a too large energy window. Indeed the value, where the fitting value converges, varies with energy. Moreover, in some cases background peaks can be present in the line-shape region, due either to natural background or beam-induced background. For example, in the region of the ground-state peak there are contamination peaks due to the presence of ^{18}O in the target, and in the region of the low-energy primaries there are many lines due to the natural radioactivity of the rocks.
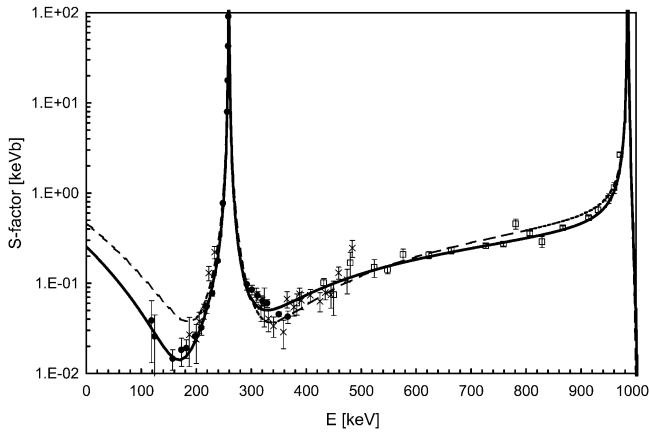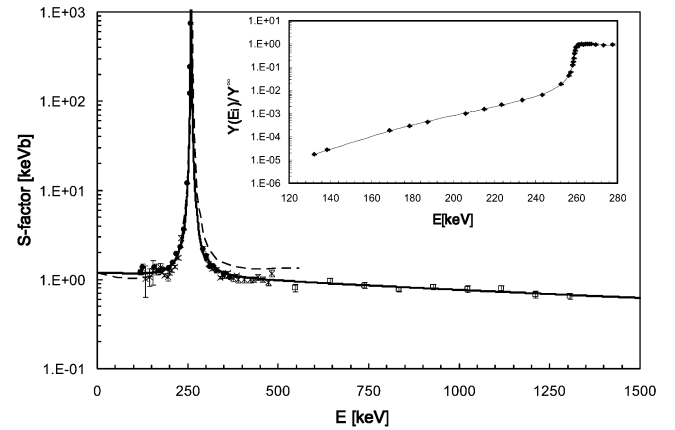
Fig. 10. The astrophysical $S_{gs}(E)$ factor for the capture to the ground state is shown from the LUNA studies (filled-in points), from previous work [5] (open squares) and from the LENA group [14] (crosses). The thick line through the data points represents our R-matrix fit, while the dashed line represents the LENA R-matrix fit.

Thus, an alternative way to analyse the data, *i.e.* simulating a thin target, is to subtract two spectra acquired at different energies. The resulting spectrum is equivalent to one acquired at the higher energy with a target thickness equal to the difference in incident energy ($\Delta = E_{max} - E_{min}$). An example is shown in fig. 9: the upper part shows the γ-spectra obtained at $E_p = 250$ keV (dark-gray area) and 240 keV (light-gray area) for the primary transition to the 6.79 MeV state; the central part shows the γ-spectrum resulting from the subtraction of both spectra, which is equivalent to a spectrum acquired at an energy of 250 keV with a target of $\Delta = 10$ keV thickness. After the final R-matrix analysis was completed, we have reinvestigated this differential method, using the R-matrix results, which is shown in the bottom part of fig. 9. Excellent agreement with the approximation shown in the upper and central parts is noted. The differential method in combination with the line-shape analysis has been used for the primary transitions.
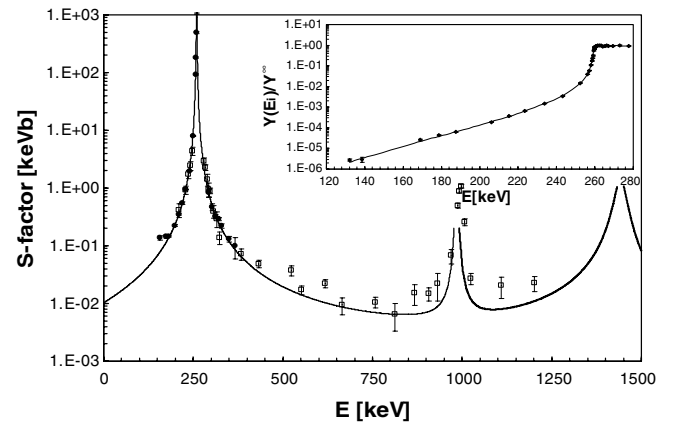
3.6 Secondary transitions

The analyses of the secondary transitions have several advantages: i) since the γ-energies of all secondary transitions are above 5 MeV, we can make full use of the advantage of an underground laboratory; ii) the expected peaks are relatively narrow (compared to the primaries) and hence the peak-to-background ratio is improved; iii) there is no efficiency correction necessary when comparing the off-resonance yield with that on-resonance; iv) the interpretation of the observed yield in combination with an 80 keV thick target is nearly identical with the integral of the cross-section from $E = 0$ to the incident energy, thus target-profile corrections are not necessary; v) angular distribution effects are expected to be negligible (sect. 3.4).

The yields of all secondary transitions were obtained by fitting the background with a linear function at the low-

Fig. 11. The astrophysical $S_{6.79}(E)$ factor for the capture to the 6.79 MeV state is shown from the LUNA studies (filled-in points), recent work [17] (open squares) and from the LENA group [14] (crosses). The insert shows the thick-target yield data for the 6.79 MeV secondary transition. The lines through the data points represent the results of our R-matrix fit. The dashed curve is scanned from [10].
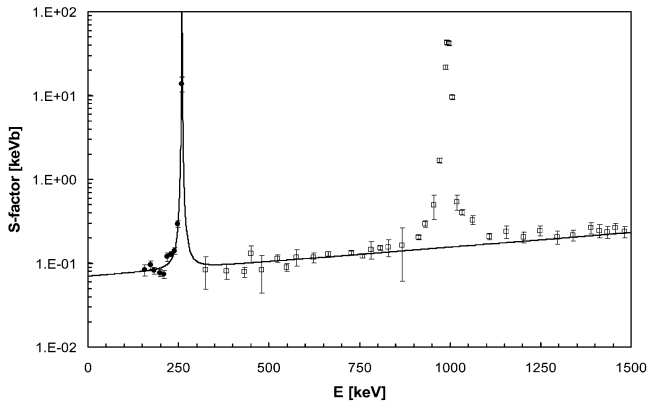

Fig. 12. The astrophysical $S_{5.18}(E)$ factor for the capture to the 5.18 MeV state is shown from the LUNA studies (filled-in points) and previous work [5] (open squares). The insert shows the thick-target yield data for the 5.18 MeV secondary transition. The lines through the data points represent the results of our R-matrix fit.

energy and high-energy sides of the peak which was then subtracted from the total peak intensity. The yield was then compared with the corresponding thick-target yield step Y^∞ at the resonance. The resulting thick-target yield curves are shown in the inserts of figs. 11, 12 and 14 for the secondary transitions $E_\gamma = 6.79, 5.18$ and 6.17 MeV, respectively. Each yield ratio corresponds to the integral from $E = 0$ to the respective incident beam energy E_i taken in the center-of-mass system. Equation (10) can thus be written:

$$\frac{Y(E_i)}{Y^\infty} = \frac{2}{\lambda^2 \omega\gamma} \int_0^{E_i} \frac{\sigma(E)b_j\eta(E_R)}{\eta(E)} dE, \qquad (13)$$

where $\omega\gamma$ are the respective values for the individual transitions of the $E_R = 259$ keV resonance. These yield ratios

Fig. 13. The astrophysical $S_{5.24}(E)$ factor for the capture to the 5.24 MeV state (only secondary transition was observed) is shown from the LUNA studies (filled-in points) and previous work [5] (open squares). The line through the data points represents the energy dependence of the DC process including the 259 keV resonance contribution.

Fig. 14. The astrophysical $S_{6.17}(E)$ factor for the capture to the 6.17 MeV state is shown from the LUNA studies (filled-in points), previous work [5] (open squares) and from the LENA group [14] (crosses). The insert shows the thick-target yield data for the 6.17 MeV secondary transition. The lines through the data points represent the results of our R-matrix fit. The dashed curve is scanned from [10].

are corrected for summing-out effects. Note that the stopping power only enters eq. (13) as a ratio and has not to be known absolutely. In principle one could also use the differential method (subtraction of the secondary peak contents from two runs with successive beam energies) to determine the energy behavior of the cross-section. However, the statistical error increases by subtracting two large numbers together with the uncertainty in the determination of the effective beam energy. Since the energy dependence of the cross-section is in principle known from the R-matrix analysis of the primaries we have adopted the method of fitting the thick target yield curve (eq. (13)) using the R-matrix analysis with a fine tuning of the fit parameters. The solid curves through the data points of the secondary transitions, the insert in figs. 11, 12 and 14, are the results of integrated R-matrix calculation.

To complete the study of the secondary peaks we have studied the 5.24 MeV (see fig. 13) transition. The 5.24 MeV state is populated by cascades through the 7.28 and 6.85 MeV states, which in turn decay 100% to the 5.24 MeV state [5]. In the 259 keV resonance the 5.24 MeV state is populated directly with 0.6% branching. At energies below this energy the primary peaks feeding the 7.28 and 6.85 MeV states were not visible in our spectra.

The results of both analyses are shown in figs. 10-14 and numerical values are given in table 2. The solid curves in the insert of figs. 10-14 are the results of integrated R-matrix calculations.

4 R-matrix analysis and discussion

The experimental results for the transition to the ground state and to the $E_x = 6.79$ MeV state were reported in [11] and an R-matrix [7,6] analysis was described for these two transitions with the results: $S_{gs}(0) = 0.25 \pm 0.06$ keV b and $S_{6.79} = 1.35 \pm 0.05$ keV b, where the quoted errors include only statistical uncertainties of the data; this error quotation was also applied below. The cross-section for all
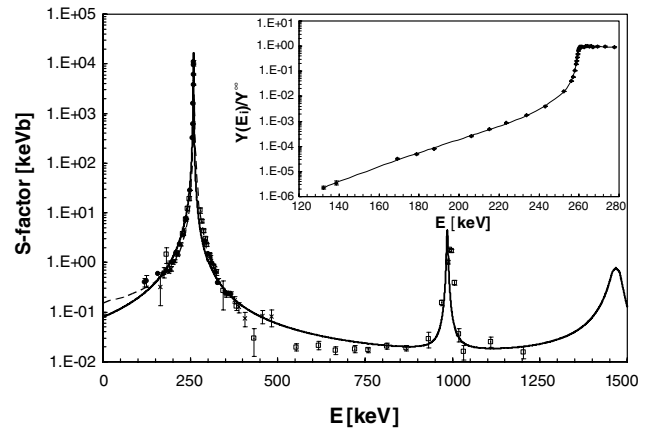
transitions to excited states can be determined via the primary and secondary transitions. The $S(E)$ determination of the primary transitions has been described in sect. 3.5 and can be directly used for an R-matrix analysis. The peak of a secondary transition for an infinitely thick target contains the integrated yield from zero energy to the respective beam energy. Thus, its interpretation requires knowledge of the energy dependence of the cross-section. This energy dependence is provided by the R-matrix fit on the primary data as a starting condition with a subsequent fine tuning of the fitting parameters. Such a procedure was used for the transitions to the 5.18, 6.17 and 6.79 MeV states. The best choice of the channel radius for fitting the transition to the ground state and 6.79 MeV state was found [11] to be a = 5.5 fm, which was used for the present R-matrix calculations.

4.1 Transition to the ground state

The data from LUNA and previous works for the ground-state capture are shown in fig. 10. We refer to the analysis described in our previous paper [11]. Briefly, the data were fitted including the $3/2^+$ sub-threshold state, the $1/2^+$, 259 keV, the $3/2^+$, 987 keV and the $3/2^+$, 2187 keV resonances as well as a background pole located at 6 MeV. For the sub-threshold state, we used the reduced width obtained from the fit of the data for the 6.79 MeV transition. The fit parameters were the Γ_γ of the subthreshold state, the 987 keV and 2187 keV resonances, the Γ_p and Γ_γ of the background pole. For the external contribution we used the ANC of [13] as a starting value. The corresponding Γ_γ value for the sub-threshold state is 0.8 ± 0.4 eV, which is in good agreement with the value from a lifetime measurement by [8] $\Gamma_\gamma = 0.41^{+0.34}_{-0.13}$ eV as well as with $\Gamma_\gamma = 0.95^{+0.60}_{-0.95}$, the value from Coulomb excitation work [9]. The minimum in

Table 2. S-factor for different capture transitions. $S(E)$ in units of keV b for transitions to E_X (MeV) states.

$E_{eff}^{(a)}$	0	5.18	5.24	6.17	6.79
118.9	0.04 ± 0.03			0.4 ± 0.1	1.2 ± 0.1
124.4	0.03 ± 0.02			0.43 ± 0.12	1.36 ± 0.12
157.0	0.015 ± 0.004	0.14 ± 0.01	0.08 ± 0.01	0.60 ± 0.03	1.36 ± 0.05
173.1	0.018 ± 0.006	0.15 ± 0.01	0.10 ± 0.01	0.60 ± 0.02	1.26 ± 0.04
182.2	0.019 ± 0.004	0.147 ± 0.007	0.08 ± 0.01	0.68 ± 0.02	1.30 ± 0.03
198.1	0.026 ± 0.003	0.226 ± 0.009	0.08 ± 0.01	1.00 ± 0.02	1.34 ± 0.03
209.5	0.032 ± 0.006	0.35 ± 0.01	0.07 ± 0.01	1.53 ± 0.03	1.55 ± 0.03
219.2	0.055 ± 0.009	0.55 ± 0.02	0.12 ± 0.01	2.31 ± 0.05	1.94 ± 0.05
229.1	0.077 ± 0.005	0.95 ± 0.01	0.13 ± 0.01	3.57 ± 0.03	2.30 ± 0.02
239.1	0.177 ± 0.006	1.98 ± 0.03	0.14 ± 0.01	7.54 ± 0.07	3.62 ± 0.05
248.6	0.77 ± 0.02	7.97 ± 0.06	0.30 ± 0.03	28.08 ± 0.13	11.98 ± 0.08
256.2	7.97 ± 0.19	93 ± 2		319 ± 7	122 ± 3
257.2	17.75 ± 0.45	182 ± 5		617 ± 16	243 ± 6
258.0	43 ± 1	492 ± 15		1586 ± 49	746 ± 23
258.4	91 ± 3	1061 ± 30		3780 ± 107	1440 ± 41
258.7	169 ± 5	1719 ± 55		6139 ± 196	2532 ± 81
259.0	293 ± 11	2575 ± 95		9488 ± 351	4514 ± 167
259.3	241 ± 10	3691 ± 157		10973 ± 467	4399 ± 187
301.5	0.08 ± 0.01	0.47 ± 0.06		1.49 ± 0.06	1.83 ± 0.09
311.4	0.073 ± 0.008	0.32 ± 0.03		0.99 ± 0.03	1.40 ± 0.05
320.9	0.063 ± 0.007	0.29 ± 0.02		0.64 ± 0.02	1.41 ± 0.03
329.1	0.060 ± 0.006	0.22 ± 0.02		0.39 ± 0.02	1.26 ± 0.02
350.3	0.045 ± 0.003	0.13 ± 0.01		0.24 ± 0.01	1.17 ± 0.02
366.8	0.043 ± 0.007	0.10 ± 0.04		0.23 ± 0.03	1.05 ± 0.04

(^{a}) Effective center-of-mass energy (in unit of keV) within the target [1].

Table 3. Values of astrophysical factor $S(0)$ from present and previous work in units of keV b.

E_X [keV]	Present	[5]	[6]	[14]	[13]
0	0.25 ± 0.06	1.55 ± 0.34	$0.08^{+0.13}_{-0.06}$	0.49 ± 0.08	0.15 ± 0.07
5183	0.010 ± 0.003				
5241	0.070 ± 0.003				
6173	0.08 ± 0.03	0.14 ± 0.05	$0.06^{+0.01}_{-0.02}$	0.04 ± 0.01	0.13 ± 0.02
6793	1.20 ± 0.05	1.41 ± 0.02	1.63 ± 0.17	1.15 ± 0.05	1.4 ± 0.2
total	1.61 ± 0.08	3.20 ± 0.54	1.77 ± 0.20	1.68 ± 0.09	1.68 ± 0.2

the S-factor shape at energy lower than 200 keV is due to an interference effect between the sub-threshold state and the nonresonant capture mechanism. The extrapolation of the S-factor is based on the energy dependence of the complete data set and not on the lowest data points. The extrapolated value of the ground-state S-factor is $S_{gs}(0) = 0.25 \pm 0.06$ keV b. Since the publication of [11] a new experiment was reported [14] with an extrapolated $S_{gs}(0) = 0.49 \pm 0.08$ keV b (table 3). The present data and those of [14] are in excellent agreement within their respective errors but the extrapolated $S_{gs}(0)$ differ by a factor of two, however still within their 2σ errors (fig. 10). The major difference in both R-matrix analyses is that in [11] the high-energy data of [5] —corrected for summing-in effects— were included in our analysis forcing the $S_{gs}(E)$

to be higher above the 259 keV resonance and lower below the resonance.

4.2 Transition to the $E_x = 6.79$ MeV state

It was found that the χ^2 of the R-matrix fit for the transition to $E_x = 6.79$ MeV state was primarily determined by the data of [5] forcing the fit to be higher than the lowest-energy data points of [11]. It was thus desirable to check the data above the $E_R = 259$ keV resonance. This experiment has been performed recently at the 4 MV Dynamitron tandem accelerator in Bochum over the energy range $E_p = 0.6$ to 1.3 MeV [17] using the setup of geometry 1 (fig. 2). The results are used together with the data

of [11] in a new R-matrix fit and are shown in fig. 11. The high-energy data are lower than those of [5] but still within the respective 2σ errors. In this case, the fit parameters for the R-matrix analysis were Γ_γ of the $E_R = 259$ keV resonance and the ANC of the 6.79 MeV state. The resulting fit of the thick target yield curve for the $E_\gamma = 6.79$ MeV secondary peak is also shown as insert in fig. 11. The new extrapolated value $S_{6.79}(0) = 1.21 \pm 0.05$ keV b is within 2σ of the value given in [11] and in excellent agreement with $S_{6.79}(0) = 1.15 \pm 0.05$ keV b from [14]. The new ANC value of $C = 4.7 \pm 0.1$ fm$^{-1/2}$ is still in excellent agreement with the ANC results [13] ($C = 5.2 \pm 0.7$ fm$^{-1/2}$) and [12] ($C = 4.6 \pm 0.5$ fm$^{-1/2}$). Also shown in fig. 11 is the R-matrix fit of [10] as a dashed curve: the fit does not reproduce the present data.

4.3 Transition to the $E_x = 5.18$ MeV state

This transition can be fitted with the inclusion of the two $J^\pi = 1/2^+$ resonances at $E_R = 259$ and 1446 keV and the $J^\pi = 3/2^+$ resonance at $E_R = 987$ keV, which is added incoherently. The result is shown in fig. 12 for the primary and secondary transitions. A small external DC contribution could be considered but has been neglected here since it amounts to less than 1% to the total S-factor. The resulting $S_{5.18}(0) = 0.010 \pm 0.003$ keV b can be compared with 0.018 ± 0.003 from [5].

4.4 Transition to the $E_x = 5.24$ MeV state

The $E_\gamma = 5.24$ MeV secondary transition was observed with a similar low intensity as the $E_\gamma = 5.18$ MeV transition. Due to the lack of detailed data, an R-matrix fit was not attempted and only a fit of an exponential representing the external DC contribution was used (fig. 13) yielding $S_{5.24}(0) = 0.070 \pm 0.003$ keV b compared to $S_{5.24}(0) = 0.064 \pm 0.002$ keV b from [5].

4.5 Transition to the $E_x = 6.17$ MeV state

The fitting of the transition to the 6.17 MeV state (fig. 14) requires an external DC contribution together with the two $J^\pi = 1/2^+$ resonances at $E_R = 259$ and 1446 keV which all interfere with each other, together with the $J^\pi = 3/2^+$ resonance at $E_R = 987$ keV added incoherently (fig. 1). Again, the data above $E_p = 350$ keV are from [5]. The best fit was obtained with the respective resonant Γ_γ widths 22.6, 70, and 10 meV. In particular, the fit at energies between the two $J^\pi = 1/2^+$ resonances is not very sensitive to the choice of the ANC but it is sensitive to this choice at the low-energy wing of the $E_R = 259$ keV resonance. The yield of the secondary transition (insert in fig. 14) is fitted best with $C = 0.2 \pm 0.1$ fm$^{-1/2}$ but is not acceptable if C exceeds 0.3 fm$^{-1/2}$. The result is within two standard deviations of [13] $C = 0.47 \pm 0.03$ fm$^{-1/2}$ and of [12] $C = 0.45 \pm 0.05$ fm$^{-1/2}$ after conversion

to the present coupling scheme. The extrapolated values $S_{6.17}(0) = 0.14 \pm 0.02$ [5] and 0.13 ± 0.02 keV b [13] are consistent with the present result $S_{6.17}(0) = 0.08 \pm 0.03$ keV b. Recently, the analysing power was measured [10] at $E_p = 270$ keV; the result together with the data of [5] led to $S_{6.17}(0) = 0.16$ keV b, which is a factor of two higher than our value. The agreement of their fit (scanned from [10]) with our data at the low-energy wing of the 259 keV resonance is quite good but seems to become too high at the high-energy side of the 259 keV resonance where the influence of the $M1$ component increases. Unfortunately, the authors [10] only show their fit up to $E_p = 330$ keV so that further conclusions are not possible. The analysis of [14] with $S_{6.17}(0) = 0.04 \pm 0.01$ keV b is a factor of two lower than the present result. Our data extend towards lower energies than those of [14] and in our R-matrix analysis an external DC contribution was included which interferes with both $J^\pi = 1/2^+$ resonances; thus, no background pole needs to be considered. Taking all extrapolations just discussed into account, the spread in $S_{6.17}(0)$ is of the order of ± 0.06 keV b which corresponds to 4% of the total $S(0)$-factor.

4.6 Total S-factor

Our present total S-factor, based primarily on R-matrix fits yields $S_{tot}(0) = 1.61 \pm 0.08$ keV b. This result is lower by 6% than the value given in [11] mainly due to the revised analysis of the transition to the 6.79 MeV state. The present result is in good agreement with [13,14] but differs in the weight of the contributions from the various transitions (table 3).
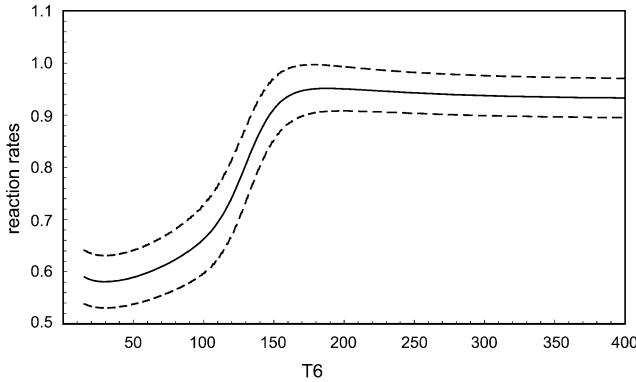
4.7 Reaction rates

We obtained an improved extrapolation for $S_{tot}(0)$ (table 3) on the basis of the present R-matrix analysis where all presently available experimental data were considered within their two σ limits. The total reaction rate for the ^{14}N(p,γ)^{15}O reaction was calculated numerically from the R-matrix results with [26]:

$$N_A \langle \sigma v \rangle = 3.7313 \cdot 10^7 \mu^{-\frac{1}{2}} T_9^{-\frac{3}{2}}$$
$$\cdot \int_0^\infty S(E) e^{(-2\pi\eta)} e^{(11.605 E/T_9)} \mathrm{d}E \qquad (14)$$

in units of cm^{3}mole^{-1}s^{-1}, where $S(E)$ is in MeV b and E in MeV and μ is the reduced mass. The resulting rates can be expressed within 0.5% using the following analytic expression for $T_9 < 2$:

$$N_A \langle \sigma v \rangle = a_1 10^7 T_9^{-2/3} \exp\left[(a_2 T_9^{-1/3} - (T_9/a_3)^2) \right]$$
$$\cdot (a_4 + a_5 T_9 + a_6 T_9^2 + a_7 T_9^3)$$
$$+ a_8 10^3 T_9^{-3/2} \exp\left[a_9 T_9^{-1} \right]$$
$$+ a_{10} 10^2 T_9^{a_{11}} \exp\left[a_{12} T_9^{-1} \right], \qquad (15)$$

Fig. 15. The reaction rate from the present work is compared with that of the NACRE compilation [26]. The dashed curves represent the uncertainty of the present reaction rate.

where:

$a_1 = 3.12$	$a_5 = -1.50$	$a_9 = -2.998$
$a_2 = -15.193$	$a_6 = 17.97$	$a_{10} = 8.42$
$a_3 = 0.486$	$a_7 = -3.32$	$a_{11} = 0.0682$
$a_4 = 0.782$	$a_8 = 2.11$	$a_{12} = -4.891$

$a_1^{low} = 2.76$	$a_5^{low} = -1.40$	$a_9^{low} = -2.998$
$a_2^{low} = -15.193$	$a_6^{low} = 15.82$	$a_{10}^{low} = 8.44$
$a_3^{low} = 0.503$	$a_7^{low} = -3.32$	$a_{11}^{low} = 0.0682$
$a_4^{low} = 0.804$	$a_8^{low} = 2.03$	$a_{12}^{low} = -4.987$

$a_1^{high} = 3.44$	$a_5^{high} = -1.59$	$a_9^{high} = -2.997$
$a_2^{high} = -15.193$	$a_6^{high} = 19.83$	$a_{10}^{high} = 8.42$
$a_3^{high} = 0.475$	$a_7^{high} = -3.30$	$a_{11}^{high} = 0.0681$
$a_4^{high} = 0.771$	$a_8^{high} = 2.18$	$a_{12}^{high} = -4.807$

The parameters labeled "low" and "high" correspond to the two σ limits of present $S_{tot}(0)$ extrapolation and include the error in the strength determination $\omega\gamma$ of the 259 keV resonance. The results are compared in fig. 15 with the rates given in the NACRE compilation [26]. They confirm the conclusion of [6] that the rate has to be reduced by nearly a factor of two at low temperatures, but it is in good agreement with NACRE [26] above $T_6 = 150$.

It can be also concluded from the present analysis that the data above the 259 keV resonance are of crucial importance for a reliable extrapolation. This finding emphasizes that one experiment alone cannot solve the problem at low temperatures and detailed analysis of the nuclear structure of ^{15}O is required.

A recent experimental determination of the total S-factor at very low energies down to $E = 70$ keV [27] is in good agreement with the present R-matrix calculations. While the extrapolation of these data to lower energies requires a detailed knowledge of the energy dependence of the various contributions to the total S-factor, this experiment [27] gives experimental certainty of the reaction rate better than 15% for $T_6 > 90$ without any extrapolation procedure. This clearly represents a major improvement in the evaluation of the reaction rate for this temperature regime.

In conclusion, with the present determination of the reaction rates we confirm the astrophysical consequences in the determination of the age of the Globular Clusters quoted in [2], and in the CNO solar-neutrino fluxes [3,4].

References

1. C. Rolfs, W.S. Rodney, *Cauldrons in the Cosmos* (University of Chicago Press, 1988).
2. G. Imbriani *et al.*, Astron. Astrophys. **420**, 625 (2004).
3. J.N. Bahcall, M.H. Pinsonneault, Phys. Rev. Lett. **92**, 121301 (2004).
4. S. Degl'Innocenti *et al.*, Phys. Lett. B **590**, 13 (2004).
5. U. Schröder *et al.*, Nucl. Phys. A **467**, 240 (1987).
6. C. Angulo, P. Descouvemont, Nucl. Phys. A **690**, 755 (2001).
7. A.N. Lane, R.G. Thomas, Rev. Mod. Phys. **30**, 257 (1958).
8. P.F. Bertone *et al.*, Phys. Rev. Lett. **87**, 152501 (2001).
9. K. Yamada *et al.*, Phys. Lett. B **579**, 265 (2004).
10. S.O. Nelson *et al.*, Phys. Rev. C, **68**, 065804 (2003).
11. A. Formicola *et al.*, Phys. Lett. B, **591**, 61 (2004).
12. P.F. Bertone *et al.*, Phys. Rev. C **66**, 055804 (2002).
13. A.M. Mukhamedzhanov *et al.*, Phys. Rev. C **67**, 065804 (2003).
14. R.C. Runkle *et al.*, Phys. Rev. Lett. **94**, 082503 (2005).
15. A. Formicola, PhD Thesis, University of Bochum (2004).
16. H. Costantini, PhD Thesis, University of Genova (2003).
17. J. Klug *et al.*, in preparation.
18. A. Formicola *et al.*, Nucl. Instrum. Methods A **507**, 609 (2003).
19. D. Bemmerer *et al.*, Eur. Phys. J. A **24**, 313 (2005).
20. F. Strieder *et al.*, Nucl. Phys. A **718**, 135c (2003).
21. F. Ajzenberg-Selove, Nucl. Phys. A **523**, 1 (1991).
22. G. Knoll, *Radiation Detection and Measurements* (John Wiley and Sons, 1996).
23. J.F. Ziegler *et al.*, SRIM program, version 2003-20, srim-org 2003 (www.srim.org).
24. M.E. Rose, Phys. Rev. **91**, 3 (1953).
25. H. Andersen, J.F. Ziegler, *The Stopping and Ranges of Ions in Matter*, Vol. **3** (Pergamon, New York, 1977).
26. C. Angulo *et al.*, Nucl. Phys. A **656**, 3 (1999).
27. A. Lemut *et al.*, submitted to Phys. Rev. Lett. (2005).